RSC Advances

PAPER

View Article Online
View Journal | View Issue

Cite this: *RSC Adv.*, 2025, **15**, 19264

Fabrication of hydroxylated norbornene foams *via* frontal polymerization for catalytic applications†

Andrew Vogler,[a] Tina Dinh,[a] Hanlin M. Wang,[b] Ghaida Aldhahri,[c] Arfa Abrar Malik[a] and Diego Alzate-Sanchez *[a]

Polymeric foams are versatile materials with direct applications in numerous fields, including insulation and heterogeneous catalysis. Existing polymeric foam production processes involve several stages, many of which are energy intensive. Herein, we report the single-step fabrication of polymeric foams using the low energy technique, frontal ring opening metathesis polymerization, and demonstrate their use as scaffolds for the deposition of palladium nanoparticles. Initially, we studied the frontal polymerization of 5-hydroxymethyl-2-norbornene monomer using the second-generation Grubbs catalyst as an initiator. In contrast with the model frontal ring opening metathesis polymerization system of dicyclopentadiene, 5-hydroxymethyl-2-norbornene is a liquid that contains hydroxyl groups capable of inhibiting the initiator. By incorporating 10 wt% *n*-pentane within resin mixtures, we successfully fabricated hydroxyl-containing foams with high porosities. The presence of hydroxyl groups enhanced the material's ability to bind and uniformly disperse palladium nanoparticles as compared to dicyclopentadiene foams. Coupled with a more hydrophilic surface, the generated foams were demonstrated as efficient catalytic scaffolds for cross-coupling reactions with activities comparable to those of free nanoparticles. Our results demonstrate that 5-hydroxymethyl-2-norbornene can be polymerized using frontal polymerization in the presence of a blowing agent to make functional foams that serve as a platform for sustainable heterogeneous catalysts development. We envision that these novel foams have potential use as scaffolds in flow chemistry.

Received 3rd March 2025
Accepted 1st June 2025

DOI: 10.1039/d5ra01510c

rsc.li/rsc-advances

Introduction

Sustainable science and engineering require lightweight, yet structurally robust materials generated with low-energy inputs and by processes that minimize the total raw resource input. In this context, polymeric foams have attracted significant interest due to their unique combination of properties, including high impact resistance, durability, stable thermal performance, and superior electrical and thermal insulation.[1–3] The diverse range of applications for these materials has driven their economic growth. As of 2023, the global polymer foam market reached a value of $135 billion, and is projected to increase by 23.9% from 2024 to 2030.[4] Polymeric foams are materials with gas voids in a solid matrix, formed by expanding gaseous or liquid blowing agents that escape from the network as it cures.[5] Typical foaming production processes (*e.g.*, batch curing, extrusion, and injection molding), however, are energy-intensive.[6] Given rising energy and environmental concerns, efficient techniques to generate foams with tailor-made cell morphologies and properties are needed.

In contrast to traditional polymerization methods, frontal polymerization (FP) rapidly converts monomer to polymer *via* a self-sustained exothermic reaction triggered by an initial stimulus. The heat generated in the polymerization provides sufficient energy to drive complete monomer consumption within a hot polymer-to-monomer interface.[7] A wide range of materials is accessible through FP.[8,9] Specifically, FP of monomer resins containing blowing agents produces cellular solids with tunable porosity and structure.[10,11] We reportedly utilized the thermomechanical gradient observed during FP to modify the cellular structure of dicyclopentadiene (DCPD) foams synthesized by frontal ring opening metathesis polymerization (FROMP), catalyzed by the second generation Grubbs complex ([(SIMes)Ru(=CHPh)(PCy_3)Cl_2]; G2).[12] While having extensively examined the connection between input parameters (*i.e.*, blowing agent type, concentration, and resin viscosity) and properties of the resultant foams, the materials were made with no intentional application, instead displaying the dynamicity of FP.

Precious metal nanoparticles (NPs) are extensively used to catalyze useful organic transformations (*e.g.*, heterogeneous

[a]*Chemistry and Chemical Biology Department, Northeastern University, Boston, MA, USA. E-mail: d.alzatesanchez@northeastern.edu*

[b]*Beckman Institute for Advanced Science and Technology, University of Illinois at Urbana-Champaign, IL, USA*

[c]*Biomedical Engineering Department, Boston University, Boston, MA, USA*

† Electronic supplementary information (ESI) available. See DOI: https://doi.org/10.1039/d5ra01510c

cross-coupling reactions).[13] Industrial utilization of NP catalysts is often hindered by challenges related to catalyst recycling and reusability.[14] NPs supported on porous materials have emerged as a prominent alternative due to their ease of handling, high recoverability, and catalytic activity maintenance.[15,16] In this regard, polymeric materials are ideal support candidates as they are inexpensive to produce and possess a wide range of functionalities to chemically elaborate on.[17] As with other porous materials, the larger surface area of polymeric foams should facilitate an enhanced NP deposition as compared to their nonporous counterparts. Polymeric supports with polar groups, including porous cellulose or polyurethane foams, have been utilized for NP deposition.[18,19] Materials comprised of Pd NPs embedded on the surface of such polymer supports competently catalyze oxidative homocouplings and nitroarene reductions.[20,21] NPs can be integrated into polymeric scaffolds using several techniques: blending metal salts or NP solutions with foam precursors, forming NPs *in situ* within pre-formed foams, or depositing NPs by dipping or spraying them onto the support.[22] Despite the advances in NPs deposition on polymeric foams, the impact of the foam's morphology on the deposition process remains underexplored.

In this work, we present the fabrication and Pd NP deposition of hydroxyl-functionalized polynorbornene foams prepared by FROMP. First, we evaluated 5-hydroxymethyl-2-norbornene (HMNB) as a competent FROMP monomer and examined the effect of the pendant hydroxyl functional group on both the polymerization process and polymer properties. We demonstrated the significance of hydroxyl functionality in the synthesis of polymers by comparing HMNB to non-hydroxyl bearing FROMP systems. Next, we included blowing agents to fabricate energy efficient foams. By subjecting polyhydroxymethylnorbornene (p(HMNB)) foams to a Pd NP solution, we demonstrated an effective deposition and uniform distribution of NPs throughout the material, attributed to the presence of hydroxyl groups. Finally, we used these materials as heterogeneous catalysts for Suzuki–Miyaura cross-coupling reactions. This solid-support strategy effectively generates highly active and recyclable catalysts, which underscores its potential as a more sustainable catalysis platform.

Results and discussion

HMNB frontal polymerization

Norbornene-based monomers have been frequently demonstrated in FROMP to readily produce polymeric species. We envisioned that hydroxyl-functionalized norbornene species would offer several advantages, including post-functionalization opportunities, increased hydrophilicity, and intermolecular interactions. HMNB was prepared by cracking dicyclopentadiene in the presence of allyl alcohol and catalytic quantities of hydroquinone. The retro-Diels–Alder reaction of dicyclopentadiene generates two equivalents of cyclopentadiene, which rapidly undergoes a [4 + 2]-cyclization reaction with allyl alcohol to form HMNB (see ESI for details, Fig. S1†). Since HMNB is a liquid at room temperature, the synthesis of polymers *via* FROMP can be accomplished without the need for liquifying agents required in other systems.[8,23] Finally, HMNB is miscible with various blowing agents, such as *n*-pentane, enabling the production of foams *via* FROMP. Initially, we attempted FROMP of HMNB using conditions previously reported for the model system of DCPD and 5-ethylidene-2-norbornene (ENB) resins (DCPD/ENB 95/5 wt%).[8,23] We prepared a 10 000 monomer/initiator ratio (M/I) sample that contains one equivalent tributyl phosphite (TBP) inhibitor with respect to G2. HMNB was mixed with G2 at room temperature, and the subsequent reaction was triggered by the application of a soldering iron. In contrast to the model system, HMNB cannot sustain FROMP in the presence of TBP but propagates in its absence (Fig. 1). To understand inhibition behavior, we performed a protorheology test of the HMNB/G2 (10 000/1) reaction mixture in the absence and presence of TBP,[24,25] observing a gelation time of 60 and 660 min for the sample without and with inhibitor, respectively (Fig. S3†). This experiment shows the ability of HMNB to inhibit G2 due to the absence of spontaneous polymerization and an observed gelation time of 60 min. Moreover, the addition of TBP increased the gelation time further, demonstrating an even greater inhibition of G2. Compared to the model system, the inhibitory advantage of HMNB prevents spontaneous polymerization without the need for exogenous inhibitors.

Based on our previous results, we studied the FROMP of HMNB/G2 (10 000/1) in the absence of TBP. The HMNB system had a frontal velocity (v_f) of 0.16 ± 0.03 mm s^{-1}, which is more than six times slower than the v_f for the conventional DCPD system reported in previous studies (~1.0 mm s^{-1}).[23,25] Moreover, we observed that the HMNB system has a maximum temperature of 164 ± 3 °C, whereas that of the DCPD system is reported as 215 °C.[23] Next, differential scanning calorimetry (DSC) of HMNB resins revealed its enthalpy of polymerization (H_p) to be 287 ± 11.2 J g^{-1}, about 100 J g^{-1} less than that of the DCPD/ENB system reported (Fig. S4†).[25] These combined results suggest that the HMNB system releases less energy than DCPD during FROMP. However, the difference in H_p does not fully

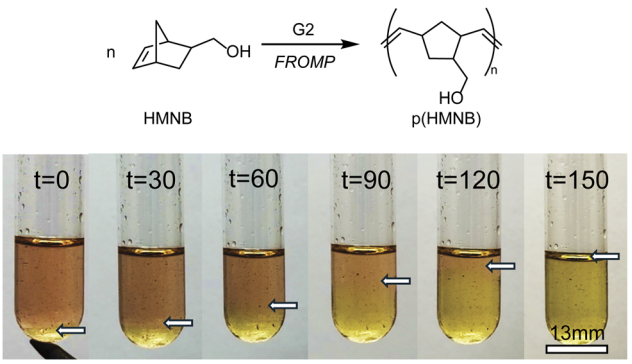

Fig. 1 5-Hydroxymethyl-2-norbornene (HMNB) Frontal Ring Opening Metathesis Polymerization (FROMP) with M/I = 10 000 HMNB (2.0 g, 16 mmol) and G2 (1.4 mg, 1.6 μmol). The bottom of the tube was touched directly with a soldering iron to initiate the reaction. Arrows denote the propagation front. The reported time is in seconds. Saturation and contrast were changed evenly for each time stamp.

account for the reduction in v_f as compared to DCPD/ENB. In literature, the FROMP of 1,5-cyclooctadiene (COD) under similar conditions has a v_f of 0.6 mm s^{-1} with an H_p of only 204 ± 5 J g^{-1}.[26] To support experimental results, computational analysis of HMNB and DCPD yielded ring strain energies of 15.4 and 19.5 kcal mol^{-1}, respectively, whereas COD is reported as 13.4 kcal mol^{-1}.[26,27] We hypothesize that the adventitious ligation of HMNB hydroxyl groups to the Ru core minimizes catalytic activity, ultimately reducing the instantaneous heat and therefore energy density generated by the polymerization under frontal conditions. Since each molecule of HMNB contains one hydroxyl group, the presence of the inhibiting species is frequent enough to prevent spontaneous polymerization while simultaneously reducing the observed energy release. Continuing with the characterization of the HMNB system, we also performed FROMP using M/I of 500, 1000, 2500, and 5000. We observed an inverse correlation between M/I and v_f (Fig. 2A), which is attributed to a less concentrated energy release, the result of decreasing the initiator amount when higher M/I ratios are employed.

HMNB is expected to form linear polymers. Consequently, we anticipated investigating their molecular weight distribution with size exclusion chromatography (SEC). After 4 days of stirring the polymers in tetrahydrofuran (THF) at room temperature with a concentration of 5 mg mL^{-1}, we observed swollen particles in the solvent instead of homogeneous solutions for each M/I (Fig. S5†). Due to unanticipated behavior in THF, other solutions were used to try and solubilize p(HMNB). HMNB polymers of M/I = 500 were chosen as solutes since they were least likely to be insoluble due to their expected lower molecular weight. Polymer samples were suspended in methanol, dimethylformamide (DMF), DMF : NH_4OH (9 : 1), and DMF : CH_3COOH (9 : 1), but we observed consistent insolubility (Fig. S6†). To further evaluate these phenomena, we synthesized HMNB polymers *via* ROMP at M/I = 100 in 20 mM $CHCl_3$ with G2. During the two-hour reaction window, the solution changed from transparent to cloudy before being quenched with ethyl vinyl ether, and an insoluble floating solid was obtained. This solid was then subjected to the same solvents noted above, but the same insolubility properties were observed. In support of these results, other norbornene species containing heteroatoms with nonbonding electrons were also found insoluble by the Matson group during ROMP.[28] The observed insolubility is characteristic of a crosslinked species, a phenomenon whose occurrence may be the result of an unintentional side reaction. We hypothesize that hydroxyl functionality interacts with the Ru core in a way that inhibits it but also permits crosslinking to occur.

Due to the limited solubility of HMNB polymers, we conducted swelling experiments in THF to assess differences in chain architecture. Remarkably, we found that polymers with a targeted lower molecular weight exhibited greater swelling. For instance, the sample with an M/I ratio of 500 displayed a swelling of 129.0 ± 3.2 wt%, whereas the sample with an M/I ratio of 10 000 exhibited a swelling of 118.3 ± 1.5 wt% (Fig. 2B and Table S1†). By assuming an equal crosslinking density across all samples, we attributed the increased swelling behavior to two main factors. First, as the polymer molecular weight increases, there is a greater likelihood of chain entanglement, leading to diminished swelling. Secondly, the increase in polymer molecular weight results in reduced free volume within the polymer matrix, further reducing swelling.[29]

We then studied the glass transition temperature (T_g) of the synthesized p(HMNB). Surprisingly, the T_g ranged from 76.9 °C to 82.3 °C in an inverse relationship with M/I (Fig. 2C and Table S2†). While we first assumed that crosslinking events were uniform across all M/I ratios, this data suggests that crosslinking is correlated with the amount of initiator. In other words, a lower M/I elevates the T_g and indicates that more crosslinking events are present as M/I decreases. However, a greater degree of crosslinking should be directly correlated to a decrease in swelling, which was not observed in the studied systems.

We argue that the swelling and T_g results can be explained as the result of a more prominent influence of chain length over crosslinking events in the HMNB system. Over the range of all M/I employed, the difference in T_g was 5.4 °C (6.6–7.0%), whereas the difference in swelling was 10.7% (8.3–9.0%). It is suggested that a large change in the M/I did not have a significant impact on crosslinking density since a small difference in T_g was observed across all M/I. However, the change in

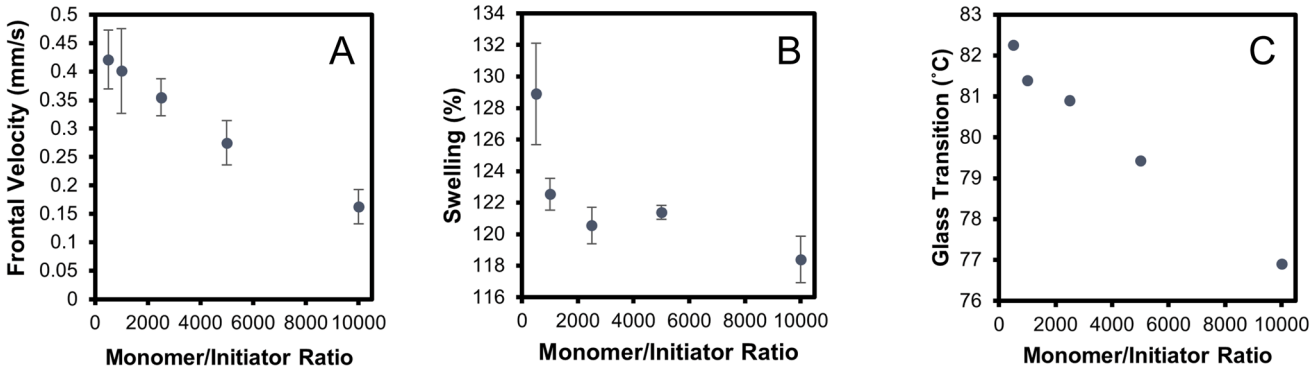

Fig. 2 (A) v_f of HMNB FROMP at various M/I ratios; (B) swelling of p(HMNB) in THF as a function of M/I ratios; (C) glass transition temperatures of p(HMNB) at different M/I ratios determined by differential scanning calorimetry.

theoretical chain length was twenty-fold from an M/I of 500–10 000. We hypothesize that for p(HMNB), a greater chain length has a stronger influence on swelling than crosslinking events. Similarly, the impact of crosslinking events on T_g could have been minimized because of this change in chain length. Although acknowledged, the possibility of a crosslinking event was not evaluated further.

We also performed a qualitative study of the soluble fraction from swelling experiments using ^{1}H NMR. In all the samples, we elucidated the predominant presence of butylated hydroxytoluene, the stabilizer used in THF. Interestingly, the soluble fractions derived from HMNB polymers of M/I = 5000 and 10 000 also exhibited the presence of HMNB, indicative of incomplete monomer conversion. Notably, a consistent signal at 5.54 ppm was observed across all samples, which we attribute to the vinylic protons of soluble HMNB polymers (Fig. S7†). The soluble fraction study indicates that only a small fraction of the polymer is soluble. Moreover, it suggests that samples prepared with the lowest initiator concentration did not fully polymerize the monomer.

Methoxy methyl norbornene frontal polymerization

Based on our previous results, we hypothesize that the hydroxyl functional groups are responsible for the observed insolubility. To further support the significance of hydroxyl functionality, we methylated HMNB to 5-methoxymethyl-2-norbornene (MMNB) (see ESI for details, Fig. S2†).[30] We then attempted FROMP of MMNB at a M/I = 500 with G2 in the absence of TBP and observed spontaneous polymerization before FROMP initiation could occur. This uncontrolled MMNB polymerization aligns with our previous discussion of G2 inhibition by HMNB.

To suppress spontaneous polymerization and perform FROMP with MMNB, we incorporated an equimolar quantity of TBP with respect to G2. The polymethoxymethylnorbornene (p(MMNB)) generated were subjected to the same solvent conditions as p(HMNB) at M/I = 500 and in each instance were soluble. Since p(MMNB) was soluble in THF, we evaluated the solution at 5 mg mL^{-1} using SEC. We observed a number average molecular weight (M_n) of 7.54 kDa and a weight average molecular weight (M_w) of 10.3 kDa, resulting in a polydispersity of 1.36 (Fig. S8†). The experimental M_n was similar to the theoretical M_n of 6.91 kDa for linear p(MMNB) at M/I = 500, supporting that FROMP is a controlled polymerization, as previously reported.[31] Although both HMNB and MMNB contain similar functionalities, this experiment demonstrates that a methoxylated group is insufficient in producing the insolubility behavior observed in the hydroxylated system. Finally, we performed a kinetic comparison between the polymerization of MMNB and HMNB (see ESI† for more details). For both HMNB and MMNB, an M/I = 100 of monomer and G2 were mixed in $CDCl_3$ at 200 mM. In the presence of MMNB, we observed a small shift in the G2 alkylidene proton from 19.141 to 19.136 ppm. In the HMNB sample, the shift was larger and resulted in a peak at 19.126 ppm (Fig. S9†). We also observed the consumption of MMNB based on the decrease in the monomer signal intensities at 6.1 and 5.9 ppm. Additionally, we observed the appearance of a new peak at 5.3 ppm, which was assigned to polymer formation. For HMNB, we did not observe the previously assigned p(HMNB) signal, and no change in signal intensity for its monomer, suggesting no polymerization had occurred (Fig. S10†). We hypothesize that the shift seen in the MMNB mixture is the result of G2 bound to growing polymer chains that were actively propagating. However, for HMNB we hypothesize that this shift, as well as the lack of p(HMNB) formation, is the result of hydroxyl ligation to the Ru core. These results support the inhibitory properties of HMNB previously observed. Collectively, the comparison between HMNB and MMNB demonstrates the significance of hydroxyl functionality on the resultant polymer synthesis and properties.

HMNB frontal foaming

With the goal of fabricating polymeric foams, we considered the resin formulation that would release sufficient energy to evaporate blowing agents with high monomer conversion. The v_f of M/I = 2500 was within the lower half of the error seen in M/I = 1000, suggesting a comparable energy release (Fig. 2A). Moreover, we did not observe a difference in the presence of unreacted HMNB from the soluble fractions of M/I = 500, 1000, and 2500 (Fig. S7†). Based on these findings, we opted to use M/I = 3500 for the fabrication of HMNB foams to minimize the usage of the initiator and maximize monomer conversion. Frontal velocity for this system was 0.34 ± 0.02 mm s^{-1}, which is within the error of the sample synthesized with an M/I ratio of 2500, suggesting a similar energy release. Additionally, we noted a maximum frontal temperature of 194 ± 3 °C (Fig. S11†), a value greater than the 164 ± 4 °C observed in the M/I = 10 000 HMNB system. This higher maximum temperature of the lower M/I system will help guarantee a more efficient evaporation of blowing agents.

For the fabrication of HMNB foams, we opted for *n*-pentane as the blowing agent owing to its low boiling point and miscibility with HMNB. HMNB/G2 was prepared at a 3500 M/I ratio, incorporating varying amounts of *n*-pentane (ranging from 10% to 40 wt%). We observed the formation of foams when utilizing *n*-pentane at concentrations up to 20 wt%. However, the formulation containing 30 wt% quenched during FROMP, and the formulation with 40 wt% failed to initiate altogether (Videos S1–S3†). Moreover, the increase of the blowing agent prolonged the initiation time of the reaction, shifting it from 47 s for the 10 wt% foam to 190 s for the 30 wt% foam. This prolonged initiation period leads to partial evaporation of the blowing agent before FROMP begins, thus impeding the intended purpose of adding more blowing agent to achieve a foam with higher porosity.

The foams obtained using 10 and 20 wt% of blowing agent were characterized using microcomputed tomography (Micro-CT). We observed macropores in both samples, but upon closer examination, we found distinct characteristics: the sample synthesized with 10 wt% *n*-pentane exhibited isolated voids dispersed throughout the structure, whereas the foam synthesized with 20 wt% *n*-pentane displayed a prominent central void surrounded by smaller voids (Fig. 3). One way to quantify the porosity of polymeric materials is by measuring the

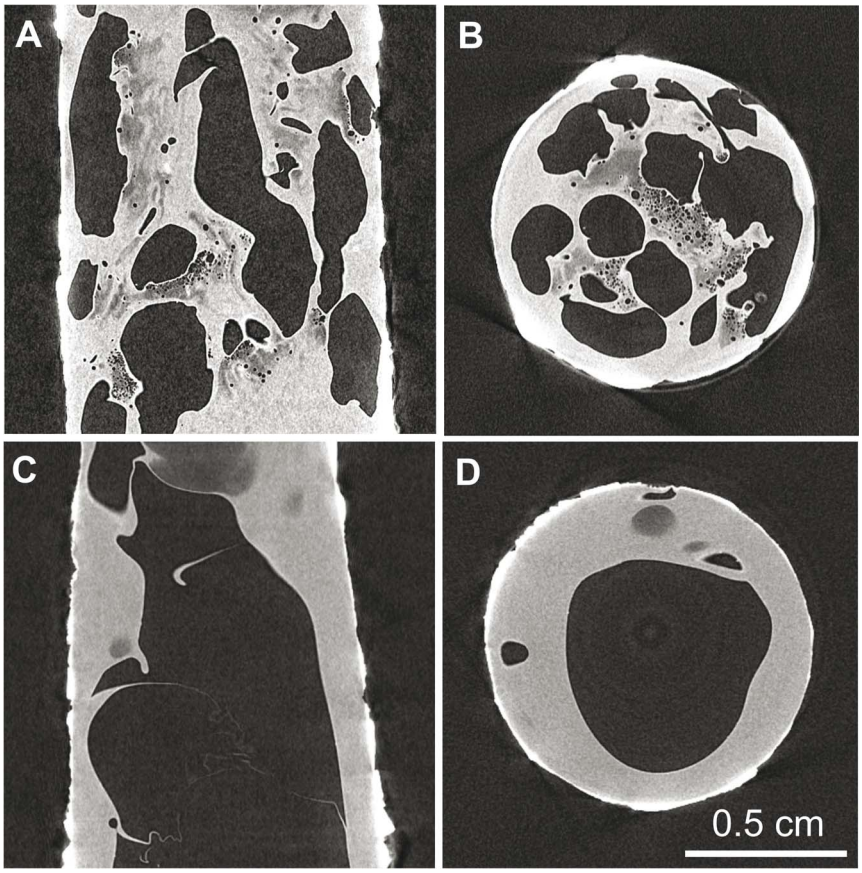

Fig. 3 Microcomputed tomography images of the HMNB foam prepared with *n*-pentane as the blowing agent. (A) Frontal cross section of the 10 wt% foam (B) superior cross section of the 10 wt% foam (C) frontal cross section of the 20 wt% foam (D) superior cross section of the 20 wt% foam.

volume fraction of the entire material. Higher volume fraction values, nearing 1.0, indicate samples with fewer pores or nonporous characteristics. This value was determined using the BoneJ plugin in ImageJ.[32] The obtained volume fractions were 0.21 and 0.096 for the foams synthesized with 10 and 20 wt% *n*-pentane, respectively. While the foam synthesized with 20 wt% *n*-pentane is more porous, its cellular structure does not resemble that of a typical foam but rather that of a polymer with a central cylindrical cavity. Additionally, an analysis of the distribution of void areas in the cross sections of the foams reveals that in the foam synthesized with 10 wt% *n*-pentane, 68.9% of the voids have an area ranging from 0.0010 to 0.051 cm^2, whereas the foam synthesized with 20 wt% *n*-pentane exhibits a bimodal distribution, with only 19.4% of the voids falling within the 0.0010–0.051 cm^2 range (Fig. S12†). Since the 10 wt% foams contained more frequent pores within this smallest measured range as well as a more robust macrostructure, we employed this formulation as the scaffold to deposit the Pd NPs.

Pd NP synthesis and deposition performance

The synthesis of Pd NPs was done following a reported protocol that results in polyvinylpyrrolidone coated NPs.[21] The nanoparticles exhibited rectangular and triangular shapes with sizes ranging between 6.3 and 17 nm (Fig. S13†). To investigate their catalytic activity, we ran a Suzuki–Miyaura cross-coupling reaction between iodobenzene and phenylboronic acid in the presence of Pd NPs. We conducted the coupling reaction employing 0.2 mol% of NPs, with reactants at a concentration of 0.05 M, maintained at 60 °C in an ethanol/water (1 : 1) mixture. We quantified the formation of biphenyl over the course of six hours using gas chromatography mass spectroscopy to determine when biphenyl production plateaued (Fig. S14†). By four hours, the formation of biphenyl starts to taper off to around 92%.

For deposition of the Pd NPs onto p(HMNB) foams (p(HMNB)-F), we explored two different methods. Method one was an *in situ* deposition where foams were incorporated into the Pd NP reaction mixture (IS-Pd@p(HMNB)-F). The second method was an *ex situ* deposition where foams were oscillated in a Pd NP suspension overnight (ES-Pd@p(HMNB)-F). The quantification of Pd NPs using inductively coupled plasma mass spectrometry (ICP-MS) showed Pd concentrations of 415 ppm and 2620 ppm for IS-Pd@p(HMNB)-F and ES-Pd@p(HMNB)-F, respectively. Following the deposition, we performed catalysis using the same reaction conditions used for free Pd NPs. The foams from method one generated no biphenyl, suggesting that the presence of polymer in the Pd NP reaction mixture affected their catalytic

activity. In contrast, the functionalized foams from method two did form biphenyl. Based on the low Pd NP concentration and lack of biphenyl production by the foams prepared with method one, we selected method two, the *ex situ* deposition, for the remaining experiments.

Next, we assessed the interactions of Pd NPs with both HMNB and the model DCPD system. We hypothesized that the hydroxyl functionality of HMNB would more positively influence Pd NP deposition as compared to the nonpolar model system as a result of its dipole interaction with the NP coating (Fig. S15†). Initially, we assessed the ability of both monomeric species to disperse Pd NPs by suspending 1 mg of NPs in 1 g of either DCPD/ENB or HMNB. In the DCPD/ENB system, the presence of black spots indicated poor dispersion and nanoparticle aggregation, whereas HMNB exhibited a homogeneous dispersion, suggesting improved nanoparticle distribution. Moreover, after 20 min we observed stable dispersion of the NPs in HMNB and settlement in DCPD/ENB (Fig. S16†). After demonstrating that HMMB more effectively disperses Pd NPs, we performed a contact angle experiment to evaluate the difference in polarity at the polymeric level between p(HMNB) and p(DCPD-*co*-ENB) using the drop shape analysis plugin in ImageJ.[33] We observed contact angles for p(HMNB) and p(DCPD-*co*-ENB) of 97.6 ± 2.9° and 111 ± 1.8°, respectively (Fig. S17†). Here, a smaller contact angle reflects a more polar surface. Next, we performed the *ex situ* Pd NPs deposition onto both p(DCPD-*co*-ENB) and p(HMNB). The concentrations of Pd were 150 ppm and 1310 ppm for Pd@p(DCPD-*co*-ENB) and Pd@p(HMNB), respectively. The heightened Pd concentration in Pd@p(HMNB) demonstrates the significance of hydroxyl functionality on Pd deposition. Finally, we synthesized model system foams at 10 wt% *n*-pentane and repeated the *ex situ* deposition to generate Pd@p(DCPD-*co*-ENB)-F. Quantification of Pd in the foams revealed concentrations of 774 ppm for Pd@p(DCPD-*co*-ENB)-F, significantly lower than the 2620 ppm measured for the Pd@p(HMNB)-F system. This finding confirms that the reduced Pd deposition observed in the model system extends to the foam structures as well. Furthermore, the effectiveness of a porous structure is evident, as Pd@p(HMNB)-F exhibited twice the concentration of Pd NPs compared to its nonporous counterpart, Pd@p(HMNB).

To better visualize the microstructure and Pd deposition of Pd@p(HMNB)-F and Pd@p(DCPD-*co*-ENB)-F, we used scanning electron microscopy (SEM) and energy-dispersive X-ray spectroscopy (EDS). SEM revealed that Pd@p(HMNB)-F had uniform pores of about 5 μm in diameter amongst well-dispersed macropores (~0.5–2 mm) (Fig. 4A and B). In contrast, Pd@p(DCPD-*co*-ENB)-F only contained macropores of similar size previously seen using Micro-CT, with no smaller pores (Fig. 4E and F). The presence of frequent and much smaller pores in Pd@p(HMNB)-F supports that HMNB foams have a greater surface area than Pd@p(DCPD-*co*-ENB)-F. This increased surface area likely contributed to the larger Pd concentrations measured in Pd@p(HMNB)-F. Furthermore, the greater surface area should also contribute positively to the scaffold's performance in catalysis. We hypothesize that the presence of smaller pores in Pd@p(HMNB)-F is due to relative differences in the polarities of HMNB and DCPD with respect to *n*-pentane. While this phenomenon is certainly beneficial and should be explored, we did not do so here. Next, EDS detected Pd NPs across both species of foam. In the Pd@p(DCPD-*co*-ENB)-F sample, aggregates of Pd NPs can be seen with a few isolated NPs (Fig. 4G and H). In contrast, fewer aggregates are seen in Pd@p(HMNB)-F with a greater level of dispersed NPs (Fig. 4C and D). The heightened dispersity of NPs seen in EDS aligns well with the dispersion testing previously done with liquid monomers. Collectively, these results demonstrate that the increased polarity introduced by HMNB functionality enhances both the dispersion and deposition of Pd NPs compared to the DCPD/ENB system.

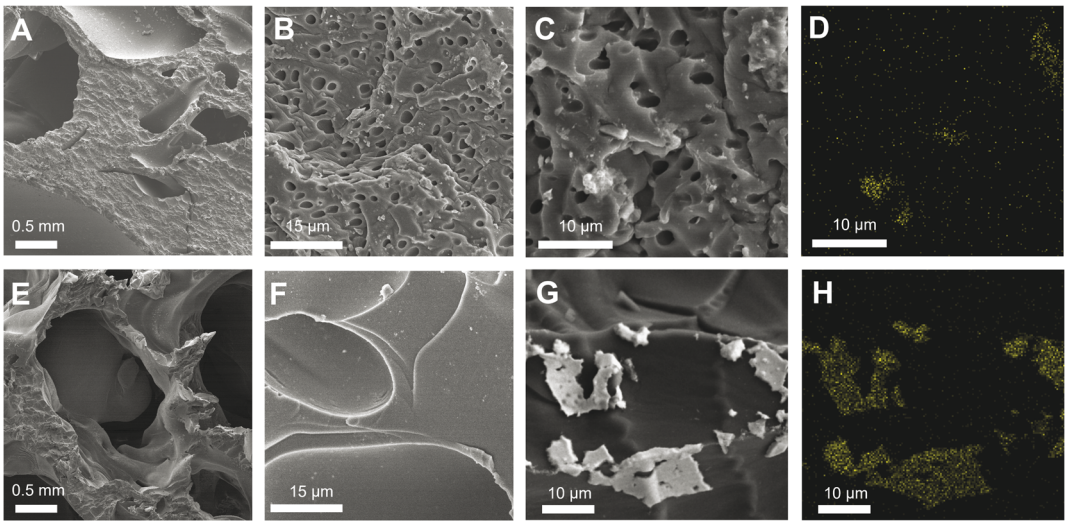

Fig. 4 SEM images of Pd@p(HMNB)-F at (A) 30×, (B) 1500×, and (C) a region corresponding to (D); (D) EDS map highlighting Pd NPs in yellow. SEM images of Pd@p(DCPD-*co*-ENB)-F at (E) 30×, (F) 1500×, and (G) a region corresponding to (H); (H) EDS map highlighting Pd NPs in yellow.

Scaffold catalysis and recyclability

Finally, we ran a Suzuki–Miyaura cross-coupling reaction between iodobenzene and phenylboronic acid using the different palladium scaffolds. The Pd NPs had the best performance with a biphenyl conversion of 87.7 ± 17.5%, followed by Pd@p(HMNB)-F with a conversion of 78.6 ± 1.89% and Pd@p(HMNB) with 75.3 ± 5.91% conversion (Fig. 5A). The Pd NPs have a turnover number (TON) and turnover frequency (TOF) of 390 and 97.4 h^{-1}, respectively. Sahoo *et al.* also performed a Suzuki–Miyaura cross-coupling reaction on their Pd NPs, where they calculated a TON of 404 and a TOF of 693 h^{-1}.[21] Our TON value is similar, but the TOF values are significantly lower. It is important to mention that these values show that their Pd NPs are more active than ours; however, our emphasis is on the role of polymer structure in the deposition of Pd NPs as opposed to the activity of the NPs themselves. A comparison of Pd@(HMNB)-F with other reported porous materials supported with Pd can also be seen in Table S3.†

Both Pd@p(HMNB)-F and Pd@p(HMNB) had lower conversions than the free Pd NPs due to the reduced accessibility of deposited NPs as compared to those free in solution. Nonetheless, the use of both Pd@p(HMNB)-F and Pd@p(HMNB) scaffolds is preferred due to the scaffolds' easy recoverability. Pd@p(HMNB)-F exhibited slightly better performance than Pd@p(HMNB). The TON and TOF were calculated for the foam to be 333 and 83.3 h^{-1}, respectively, which is not significantly different from the free Pd NPs. It is noteworthy that although the levels of catalysis were similar in both p(HMNB) scaffolds, Pd@p(HMNB)-F is a porous structure that requires less solid material to achieve a better performance. This quantity of solid material is further reduced when considering that the porous structure also contains a higher Pd concentration. The model system, Pd@p(DCPD-*co*-ENB)-F, had a biphenyl conversion of 32.6 ± 51.1%. The large deviation in biphenyl production reflects the heterogeneous distribution of aggregated Pd NPs in Pd@p(DCPD-*co*-ENB)-F previously observed in EDS (Fig. 4G and H). Together, the higher and more consistent production of biphenyl by Pd@p(HMNB)-F, compared to the other systems, supports its superiority as a catalytic scaffold. This advantage arises from Pd@p(HMNB)-F requiring less solid material to achieve high conversion levels, higher Pd concentration, and improved Pd NP dispersion—contrasting with the limitations observed in the HMNB polymer and DCDP/ENB scaffolds.

The ability to reuse supported heterogeneous catalysts is a crucial aspect that enhances their value for industrial applications. As such, we examined the recoverability and reusability of our supported catalyst in the Suzuki–Miyaura reaction between iodobenzene and phenylboronic acid under identical conditions. After each cycle, the foam was extracted, cleaned with dichloromethane, and subsequently dried in the vacuum oven overnight before initiating another round. Pd@p(HMNB)-F demonstrated reusability for two cycles, with a consistent biphenyl conversion of 79%. However, in the third cycle, biphenyl conversion drops to 45% and then 12% in the subsequent cycle (Fig. 5B). To evaluate this drop in performance, ICP-

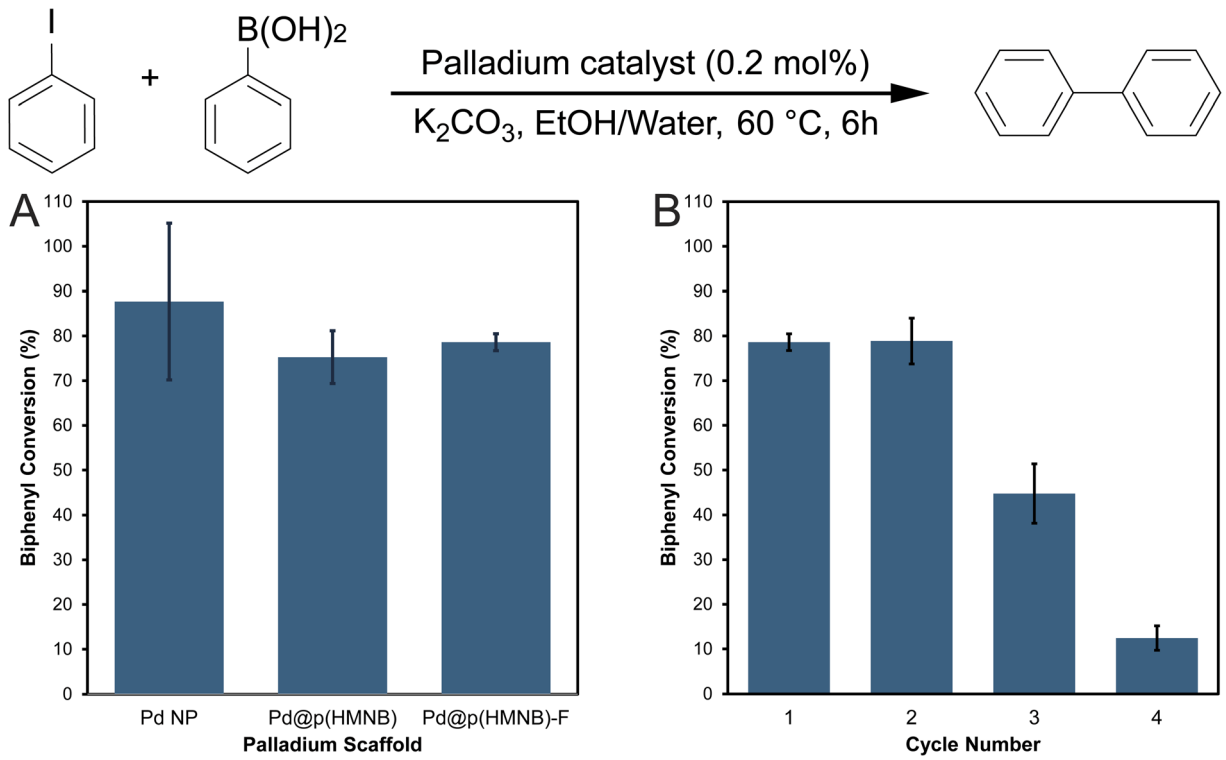

Fig. 5 (A) Biphenyl produced during Suzuki–Miyaura coupling reaction after 4 hours using palladium nanoparticles (Pd NP), *ex situ* palladium deposited HMNB polymer (Pd@p(HMNB)), and *ex situ* palladium deposited HMNB foam (Pd@p(HMNB)-F). (B) Biphenyl produced after 4 hours using the same Pd@p(HMNB)-F for four consecutive cycles.

MS revealed that after the fourth cycle of catalysis, Pd@p(HMNB)-F had 1638 ppm Pd, 62.5% of the initial amount. This result aligns well with a decrease in biphenyl conversion. However, the 12% biphenyl conversion of the fourth cycle demonstrated a disproportionately lower conversion at 1638 ppm as compared to the sample which had 79% conversion at 2620 ppm Pd. Therefore, the drop in conversion seen is not only the effect of a decrease in Pd NPs on the foam's surface, but is also likely a decrease in the total number of active or accessible Pd NPs.

As a control, the same experiment was done with the model system Pd@p(DCPD-*co*-ENB)-F, which also showed decreasing biphenyl production after each cycle and no biphenyl production during the third cycle (Fig. S18†). Although Pd@p(HMNB)-F has a higher concentration of Pd than Pd@p(DCPD-*co*-ENB)-F, its interactions with the Pd NPs are insufficient to enable multiple rounds of use. However, even after three cycles of use, Pd@p(HMNB)-F achieved a biphenyl production of 45%, exceeding the initial 32.6% yield of the model system. This highlights the advantage of hydroxyl functionality in facilitating Pd NP deposition. In future work, we will explore additional functional groups to further enhance the affinity of Pd NPs to the material's surface, improving recyclability and catalytic performance.

Conclusions

In this study, we showcased the application of frontal polymerization in synthesizing p(HMNB) foams. The ROMP of HMNB under frontal conditions varied in comparison with the DCPD/ENB model system due to its unique G2 inhibitory characteristics. Once synthesized, HMNB linear polymers displayed unexpected insolubility, a unique outcome of a hydroxylated species that disappears upon methylation. Further reaction optimization allowed for the generation of polymeric foams by incorporating blowing agents. Specifically, the inclusion of 10 wt% *n*-pentane as a blowing agent resulted in the fabrication of porous monoliths with uniformly distributed voids. Additionally, an unexpected advantage of p(HMNB) foams was seen in that pores of 5 microns in diameter were observed, suggestive of an increased surface area absent in the DCPD-*co*-ENB system foams. We then demonstrated that post-functionalization of these foams with Pd NPs was enhanced by a porous structure in addition to the polymer's hydroxyl functionality. In a Suzuki–Miyaura cross-coupling reaction, Pd functionalized p(HMNB) foams displayed greater product conversion and improved recyclability as compared to the other frontally cured scaffolds that were absent of either hydroxyl functionality or micron-sized pores. These results highlight the significance of using a porous, hydroxylated polymer in catalysis. Collectively, our research extends the utility of FP in constructing cellular structures and demonstrates the versatility of our novel foaming method beyond conventional monomers used in FROMP. This approach facilitates the creation of materials with tailored properties, particularly in catalysis. Our vision for these functionalized foams is that they serve as a new platform for the development of sustainable chemistry reactors, enabling the repeated and continuous transformation of reactants into valuable products.

Data availability

The data supporting this article have been included as part of the ESI.†

Author contributions

AV, TD, and DAS wrote the manuscript. AV performed monomer synthesis, foaming, and deposition experiments; TD performed catalysis experiments; HMW performed the Micro-CT imaging and monomer synthesis. GA performed preliminary foaming and catalysis experiments; AAM performed ring strain energy computations; DAS designed and directed the project. All authors provided critical feedback, helped shape the research, analysis, and manuscript, and have approved the final version of this manuscript.

Conflicts of interest

There are no conflicts of interest to declare.

Acknowledgements

The authors acknowledge the Northeastern University NMR Core Facility for staffing and instrumentation support. This work used an NMR spectrometer funded by National Institutes of Health SIG grant S10OD032452. The content is solely the responsibility of the authors and does not necessarily represent the official views of the NIH. This work was completed in part using the Discovery cluster, supported by Northeastern University's Research Computing team. This work also used the Boston Electron Microscopy Center at Northeastern University and the Microscopy Suite of the Beckman Institute for Advanced Science and Technology at the University of Illinois at Urbana-Champaign. Dr Benjamin A. Suslick is deeply thanked for the insightful proofreading of the manuscript.

References

1 G. Wu, P. Xie, H. Yang, K. Dang, Y. Xu, M. Sain, L.-S. Turng and W. Yang, *J. Mater. Sci.*, 2021, **56**, 11579–11604.
2 A. Kausar, *Polym.-Plast. Technol. Eng.*, 2018, **57**, 346–369.
3 R. K. Gupta, *Polymeric Foams: Applications of Polymeric Foams (Volume 2)*, American Chemical Society, 2023.
4 G. V. Research, *Polymer Foam Market Size, Share & Trends Analysis Report by Type (PC, PC/ABS, PET, PS, PP, ABS), by Application (Packaging, Building & Construction, Furniture & Bedding, Automotive, Rail), by Region, and Segment Forecasts, 2024–2030*, 2023.
5 S.-T. Lee, C. B. Park and N. S. Ramesh, *Polymeric Foams: Science and Technology*, CRC Press, Boca Raton, 2006.
6 T. Standau, C. Zhao, S. Murillo Castellón, C. Bonten and V. Altstädt, *Polymers*, 2019, **11**, 306.

7 B. A. Suslick, J. Hemmer, B. R. Groce, K. J. Stawiasz, P. H. Geubelle, G. Malucelli, A. Mariani, J. S. Moore, J. A. Pojman and N. R. Sottos, *Chem. Rev.*, 2023, **123**, 3237–3298.
8 I. D. Robertson, M. Yourdkhani, P. J. Centellas, J. E. Aw, D. G. Ivanoff, E. Goli, E. M. Lloyd, L. M. Dean, N. R. Sottos, P. H. Geubelle, J. S. Moore and S. R. White, *Nature*, 2018, **557**, 223–227.
9 K. Bansal, J. A. Pojman, D. Webster and M. Quadir, *ACS Macro Lett.*, 2020, **9**, 169–173.
10 J. Daguerre-Bradford, D. S. Camarda, A. J. Lesser, A. M. Cristadoro, M. Linnenbrink and M. Schütte, *J. Appl. Polym. Sci.*, 2024, **141**, e55399.
11 Q. Z. Yan, G. D. Lu, W. F. Zhang, X. H. Ma and C. C. Ge, *Adv. Funct. Mater.*, 2007, **17**, 3355–3362.
12 D. M. Alzate-Sanchez, M. M. Cencer, M. Rogalski, M. E. Kersh, N. Sottos and J. S. Moore, *Adv. Mater.*, 2022, **34**, 2105821.
13 I. Saldan, Y. Semenyuk, I. Marchuk and O. Reshetnyak, *J. Mater. Sci.*, 2015, **50**, 2337–2354.
14 W. J. Stark, P. R. Stoessel, W. Wohlleben and A. Hafner, *Chem. Soc. Rev.*, 2015, **44**, 5793–5805.
15 R. J. White, R. Luque, V. L. Budarin, J. H. Clark and D. J. Macquarrie, *Chem. Soc. Rev.*, 2009, **38**, 481–494.
16 C. R. Kim, T. Uemura and S. Kitagawa, *Chem. Soc. Rev.*, 2016, **45**, 3828–3845.
17 R. Poupart, D. Grande, B. Carbonnier and B. Le Droumaguet, *Prog. Polym. Sci.*, 2019, **96**, 21–42.
18 Z. Farrokhi, A. Ayati, M. Kanvisi and M. Sillanpää, *J. Appl. Polym. Sci.*, 2019, **136**, 46997.
19 G. Biliuta and S. Coseri, *Coord. Chem. Rev.*, 2019, **383**, 155–173.
20 S. Frindy, A. Primo, M. Lahcini, M. Bousmina, H. Garcia and A. El Kadib, *Green Chem.*, 2015, **17**, 1893–1898.
21 L. Sahoo, S. Mondal, N. C. Beena, A. Gloskovskii, U. Manju, D. Topwal and U. K. Gautam, *ACS Appl. Mater. Interfaces*, 2021, **13**, 10120–10130.
22 R. C. Fierascu, E.-M. Lungulescu, I. Fierascu, M. S. Stan, I. C. Voinea and S. I. Dumitrescu, *Polymers*, 2023, **15**, 4570.
23 I. D. Robertson, L. M. Dean, G. E. Rudebusch, N. R. Sottos, S. R. White and J. S. Moore, *ACS Macro Lett.*, 2017, **6**, 609–612.
24 M. T. Hossain and R. H. Ewoldt, *J. Rheol.*, 2024, **68**, 113–144.
25 J. J. Lessard, E. B. Mejia, A. J. Kim, Z. Zhang, M. G. Berkey, Z. S. Medina-Barreto, R. H. Ewoldt, N. R. Sottos and J. S. Moore, *J. Am. Chem. Soc.*, 2024, **146**, 7216–7221.
26 L. M. Dean, Q. Wu, O. Alshangiti, J. S. Moore and N. R. Sottos, *ACS Macro Lett.*, 2020, **9**, 819–824.
27 P. R. Khoury, J. D. Goddard and W. Tam, *Tetrahedron*, 2004, **60**, 8103–8112.
28 S. J. Scannelli, A. Paripati, J. R. Weaver, C. Vu, M. Alaboalirat, D. Troya and J. B. Matson, *Macromolecules*, 2023, **56**, 3848–3856.
29 D. Segiet, R. Jerusalem, F. Katzenberg and J. C. Tiller, *J. Polym. Sci.*, 2020, **58**, 747–755.
30 S. D. Drouin, F. Zamanian and D. E. Fogg, *Organometallics*, 2001, **20**, 5495–5497.
31 D. M. Alzate-Sanchez, C. H. Yu, J. J. Lessard, J. E. Paul, N. R. Sottos and J. S. Moore, *Macromolecules*, 2023, **56**, 1527–1533.
32 R. Domander, A. Felder and M. Doube, *Wellcome Open Res.*, 2021, **6**, 37.
33 A. F. Stalder, G. Kulik, D. Sage, L. Barbieri and P. Hoffmann, *Colloids Surf., A*, 2006, **286**, 92–103.